A New Free-Fall Profiler for Measuring Biophysical Microstructure

FABIAN WOLK*

System Division, Alec Electronics Co. Ltd., Kobe, Japan

HIDEKATSU YAMAZAKI AND LAURENT SEURONT+

Department of Ocean Science, Tokyo University of Fisheries, Tokyo, Japan

ROLF G. LUECK

Centre for Earth and Ocean Research, University of Victoria, British Columbia, Canada

(Manuscript received 17 November 2000, in final form 12 October 2001)

ABSTRACT

This paper evaluates the performance of a newly developed free-falling microstructure profiler. The instrument is equipped with standard turbulence sensors for measuring turbulent velocity shear and temperature gradient, as well as bio-optical sensors for measuring in situ chlorophyll and turbidity variations. Simultaneous measurements with this profiler and an acoustic Doppler velocimeter were carried out in a flow tank, and data from both instruments agreed well. Turbulence spectra computed from both instruments agreed with the Kolmogorov inertial subrange hypothesis over approximately two decades in wavenumber space. Data from field tests conducted with the profiler showed that turbulence spectra measured in situ agreed with the empirical Nasmyth spectrum when corrections were made for the shear probe's spatial averaging. Dissipation rates as low as 5×10^{-10} W kg^{-1} were resolved when certain precautions were taken to avoid spectral bias caused by instrument vibrations. By assuming a universal form of the turbulence spectrum, turbulent kinetic energy dissipation rates below 5×10^{-10} W kg^{-1} can be estimated. The optical sensors resolved centimeter-scale structures of in vivo fluorescence and backscatter in field measurements.

1. Introduction

Four decades ago, plankton and other biological matter were often detrimental to the measurement of oceanic small-scale turbulence. Algae buildup or plankton collisions with the turbulence probes would frequently contaminate the measured signals or even break the delicate probes, and researchers tried to avoid measuring in regions of high biological activity (Stewart and Grant 1999). Recently, the interaction of the planktonic ecosystem and turbulence has become an area of active research (e.g., Rothchild and Osborn 1988; Yamazaki et al. 1991; Kørboe 1997; Sundby 1997; Denman and Gargett 1995; Gargett and Marra 2002; Yamazaki 1993; Yamazaki et al. 2002), and researchers now strive to obtain simultaneous measurements of turbulence and small-scale distributions of biomass in biologically active waters (Seuront et al. 1999).

The measurement of turbulence in the open ocean is almost as much art as it is science, requiring specialized sensor platforms that are difficult to operate, complex data processing, and careful data analysis. The sensor platforms must be designed to suppress high-frequency vibrations, which can contaminate the measured turbulent velocity shear signal to an extent that renders the measurement useless. The turbulence sensors are fragile and are easily destroyed by the rough handling that is common (or inevitable) on impetuous ships. A trained ''eye'' is needed to detect spots of bad data resulting from the collisions of the velocity sensor with plankton and other objects in the marine environment. Finally, the estimation of the dissipation rate of turbulent kinetic energy from the ''cleaned'' data involves many computational steps. As a result of these difficulties, the measurement of microstructure turbulence was in the past limited to a number of specialized research groups.

This paper presents the newly developed Turbulence Ocean Microstructure Acquisition Profiler (TurboMAP),

*Current affiliation: Rockland Oceanographic Services, Inc., Victoria, British Columbia, Canada.

+Current affiliation: Station Marine de Wimereux, Université des Science et Technologies de Lille, Lille, France.

Corresponding author address: Fabian Wolk, Rockland Oceanographic Services, Inc., 4–1617 Rockland Ave., Victoria, BC V8S 1W6, Canada.
E-mail: fabian@wolk.org

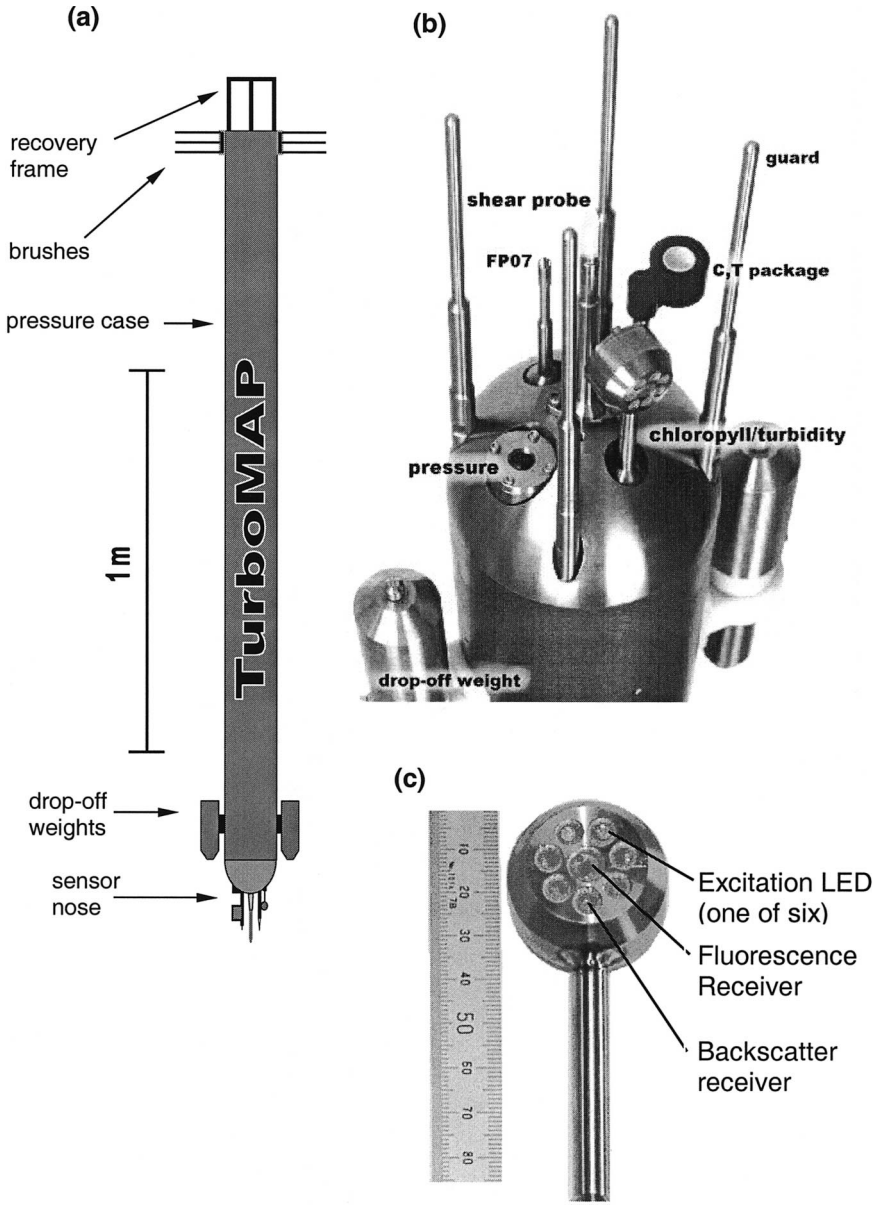

FIG. 1. Illustrations of the TurboMAP profiler: (a) schematic overview of the profiler; (b) the sensor nose; (c) the chlorophyll/turbidity sensor, the numbers on the ruler are mm.

which enables us to routinely measure physical and bio-optical microstructure. The instrument combines traditional turbulence sensors (shear probes and fast response thermistors) and a new backscatter fluorometer capable of resolving centimeter-scale distributions of chlorophyll fluorescence and turbidity. The instrument, the data acquisition system, and the sensors are described in the following section. Section 3 describes results from extensive laboratory and field experiments that were conducted to evaluate the instrument's performance and to establish the response and resolution of the sensors. The data from field trials are described in section 4. The last section summarizes the results of the tests.

2. Instrumentation

a. TurboMAP system description

TurboMAP (Fig. 1a) is a quasi-free-falling instrument that measures turbulent parameters ($\partial u/\partial z$ and $\partial T/\partial z$), bio-optical parameters (in vivo fluorescence and backscatter), and hydrographic parameters (C, T, D). In its current configuration, TurboMAP carries seven environmental sensors and a three-axis accelerometer that measures tilt and vibrations (Table 1). The environmental sensors are mounted on a parabolically shaped titanium nose (Fig. 1b) so that they are in the undisturbed flow and not affected by flow blockage. The tur-

bulent velocity fluctuations are measured with a standard shear probe, which is described in the next section. If required, a second shear probe can be added for redundancy. Conductivity (C) and temperature (T) are measured with a combined C–T sensor consisting of a platinum wire thermometer and an inductive conductivity cell. Depth is measured with a semiconductor strain gauge pressure transducer, and the instrument's sinking velocity is computed from the rate of change of the pressure signal. All sensors are sampled at a rate of 256 Hz and the readings are stored internally in nonvolatile memory. (Another version of the instrument transmits the data in real time to a shipboard data acquisition computer, but this instrument model is not discussed in this paper.)

The sensor accuracies listed in Table 1 are based on values quoted by the manufacturers. The accuracy of the FP07 thermistor is determined by the accuracy of the platinum wire thermometer (as described in section 2c). The listed sensor resolutions are based on noise level observations of quiescent field data. The lowest dissipation rate that can be resolved with the instrument (see section 4b) determines resolution of the shear probe.

Four 0.25-m-long titanium prongs project forward from the sensor nose and guard the sensor package against accidental damage during deployment and recovery. The stings can be replaced with a guard cage similar to the one presented by Dewey et al. (1987), which provides additional sensor protection and makes it possible to land the profiler on the ocean floor for bottom boundary layer measurements.

The aluminum pressure case is 2 m long and 0.15 m in diameter and contains the signal conditioning and data acquisition electronics. Fully equipped, the instrument weighs 35 kg in air and 3 kg in water, and descents with a nominal sinking velocity of 0.5 m s^{-1}.

A 5-mm-diameter Kevlar rope is attached as a tether and used to bring the instrument back to the surface at the end of each cast. In case of tether failure, a pair of expendable weights are automatically released below a preselected depth. The instrument is deployed with a special winch (manufactured by ISW Wassermesstechnik), which is mounted on the ship's gunwale. In profiling mode, the winch operator adjusts the drum speed so that the rope is paid out slightly faster than the instrument decents. This procedure ensures that the instrument is decoupled from the ship motion. At the end of the profile, the winch is reversed and the instrument is rapidly returned to the surface.

b. Shear probe

A shear probe is used to measure turbulent velocity fluctuations. This type of probe is the standard sensor for in situ dissipation-scale shear measurements, and the probe's operating principle, calibration, signal handling, and limitations are described in many publications (e.g., Osborn and Crawford 1980; Lueck et al. 1997; Gregg 1999). The probe used on TurboMAP is almost exactly the same size and shape as the so-called Osborn probe described by Ninnis (1984). The piezo-ceramic sensing element is encased in a Teflon sheath, which makes it impervious to water. When subjected to a pressure of 500 dbar, the resistance across the piezoceramic remains above 5×10^{10} Ω for at least 3 months. The probe is mounted on a 100-mm stainless steel sting in the center of the sensor nose. The probe signal is buffered and differentiated and then passed through a fourth-order Butterworth antialiasing filter with a cutoff frequency of 128 Hz (Fig. 2a). The analog differentiator turns the signal into one proportional to the rate of change of velocity, $\partial u/\partial t$ (or $\partial v/\partial t$). This signal is recorded and can later be converted to vertical velocity shear using Taylor's frozen field assumption:

$$\frac{\partial u}{\partial z} = \frac{1}{W}\frac{\partial u}{\partial t}, \tag{1}$$

where W is the speed of the oncoming flow (i.e., the sinking velocity of the instrument).

The characteristics of the differentiator circuit deviate from those of an ideal differentiator because of electronic component tolerances and the limiting of bandwidth required for circuit stability. To account for this deviation, the circuit is calibrated by measuring its response $G(f)$ to a swept-sine input. This response is then compared to the response $H_0(f) = 2\pi f$ of an ideal differentiator. Frequency spectra derived from the measured shear signal are then corrected for the differentiator characteristics by dividing them by

$$H_e^2(f) = |G(f)/H_0(f)|^2 \tag{2}$$

before further processing. An example of a measured $H_e^2(f)$ is shown as asterisks in Fig. 3.

The portion of the shear probe that can bend and respond to a cross-stream velocity fluctuation is 10 mm and, thus, the probe performs a spatial average over scales of order of 10 mm. For simple (uniform) spatial averaging, the cutoff or half-power wavelength is about twice this length, that is, $\lambda_c \approx 0.02$ m. Both the ''cutoff'' wavenumber and the form of the response of the probe are not yet well established. After comparing measured spectra against the Nasmyth empirical spectrum, Oakey (1982) suggested

$$H_c^2(k) = \frac{1}{1 + (k/k_c)^n}, \tag{3}$$

where $k_c = \lambda_c^{-1} = 50$ cpm is the half-power (cutoff) point. For $n = 2$ the response function results in a single-pole filter response. Ninnis (1984) compared the signals from a shear probe and a laser Doppler anemometer in grid turbulence and derived a half-power point of 72 cpm. However, at high wavenumbers the Ninnis response is not consistent with shape of observed spectra in highly turbulent regions; no spectrum has ever shown the null response predicted by Ninnis (Gregg 1999).

TABLE 1. Parameters measured with TurboMAP, sensor types, and sensor accuracy and resolution. All sensors sampled at 256 Hz. Units parts per billion (ppb) are equivalent to $\mu g l^{-1}$ of chlorophyll *a* (Wolk et al., 2001). Units parts per million (ppm) are based on sensor calibration against Kaolin particles.

Parameter	Type	Accuracy	Resolution
Velocity shear	Shear probe	5%	$\approx 1 \times 10^{-4}$ s^{-1}
High-resolution temperature	FP07 thermistor	0.01°C	$<1 \times 10^{-4}$°C
Low-resolution temperature	Platinum wire thermometer	0.01°C	1×10^{-3}°C
Conductivity	Inductive cell	0.002 S m^{-1}	2×10^{-4} S m^{-1}
Pressure	Semiconductor strain gauge	0.5%	1×10^{-2} db
Chlorophyll	Fluorescence	0.5 ppb	5×10^{-3} ppb
Turbidity	Backscatter	1 ppm	5×10^{-3} ppm
Acceleration (*X, Y, Z*)	Solid-state fixed mass	1%	5×10^{-4} G

Macoun and Lueck (2002, manuscript submitted to *J. Atmos. Oceanic Technol.*) operated two shear probes in a very turbulent tidal channel. One probe was identical to the probe used here while the other was a little more than half as big and of the same shape. The best spectral agreement was derived using a single-pole form ($n = 2$) and a cutoff λ_c of 48 and 89 cpm for the larger and smaller probes, respectively. The uncertainty is about 10% and, thus, we use $k_c = 50$ cpm and $n = 2$ (Fig. 3). Measured shear spectra, $\psi(f)$, are converted to wavenumber spectra using

$$\psi(k) = \psi(f)W \quad \text{and} \quad k = f/W, \tag{4}$$

and then corrected for the probe response by dividing these spectra by (3).

c. Temperature gradient sensor

Microstructure temperature fluctuations are measured with a fast thermistor (FP07), located 60 mm from the shear probe. The thermistor signal is amplified, then combined with its time derivative (prewhitening) to enhance the signal resolution (Mudge and Lueck 1994), and low-pass filtered to avoid aliasing (Fig. 2b). An example of the improvement in temperature resolution that is achieved through the prewhitening process is shown in Fig. 4. The data were recorded in the surface boundary layer of the Kuroshio. In the depth range around 20 m, the enhanced temperature signal reveals centimeter-scale fluctuations smaller than $O(10^{-4})$°C. In comparison, the platinum wire thermometer shows only bit noise in this region. Though highly sensitive, the FP07 lacks long-term stability; therefore, no absolute calibration of the sensor is performed prior to deployment. The FP07 signal is calibrated during postprocessing by second-order regression against the signal of the platinum wire thermometer.

d. Bio-optical sensors

Certain aspects of biological activity, such as fluorescence intensity and the concentration of light-scattering particles, are quantified with a combined high-resolution chlorophyll/turbidity sensor (Fig. 1c). The chlorophyll concentration is determined by measuring the fluorescent response to excitation by light with a wavelength band of 400–480 nm. The excitation is provided by six light emitting diodes (LEDs) that are placed on a circumference of 20-mm diameter. Their light is collimated and focused onto a point 15 mm in front of a photodiode, located in the center of the diode ring. The photodiode has a 640–720-nm bandpass filter. Turbidity is determined from the intensity of backscatter of the excitation light. The backscatter receiver is located

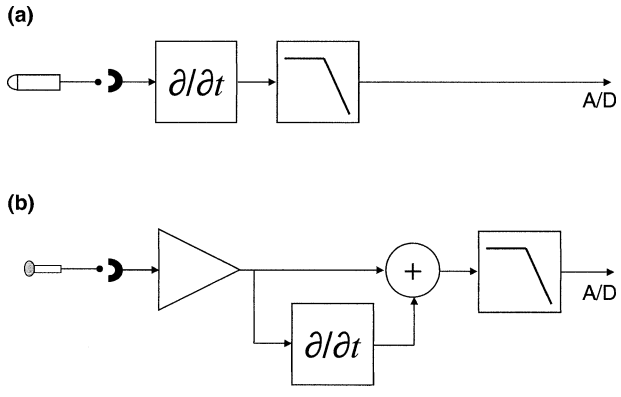

FIG. 2. Block diagrams of the signal conditioning electronics for (a) the shear probe and (b) the FP07 thermistor. The boxes containing "$\partial/\partial t$" represent differentiators, those containing a downward-sloping line represent low-pass filters. The triangle represents an amplifier.

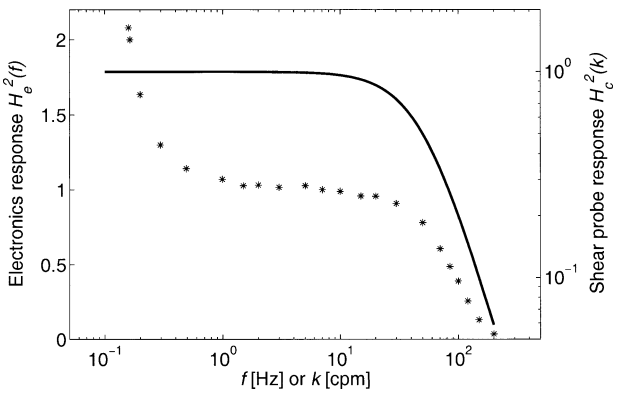

FIG. 3. Typical frequency response $H_e^2(f)$ of the differentiator circuit (shown as *) and the assumed wavenumber response of the shear probe $H_c^2(k)$ for $k_c = 50$ cpm.

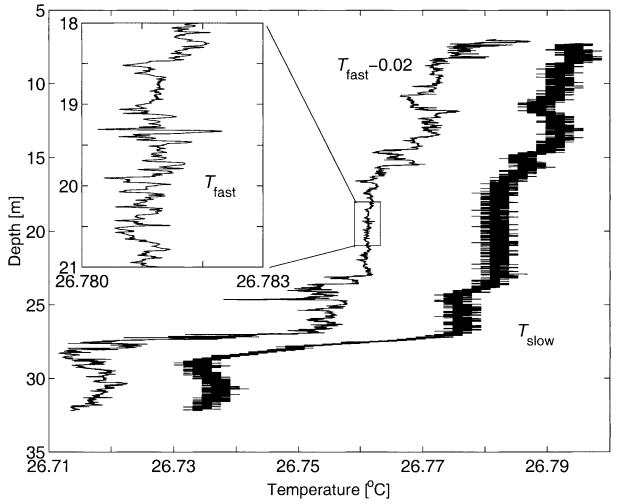

FIG. 4. High-resolution temperature signal (T_{fast}) from the FP07 thermistor with prewhitening compared to the platinum wire thermometer signal (T_{slow}).

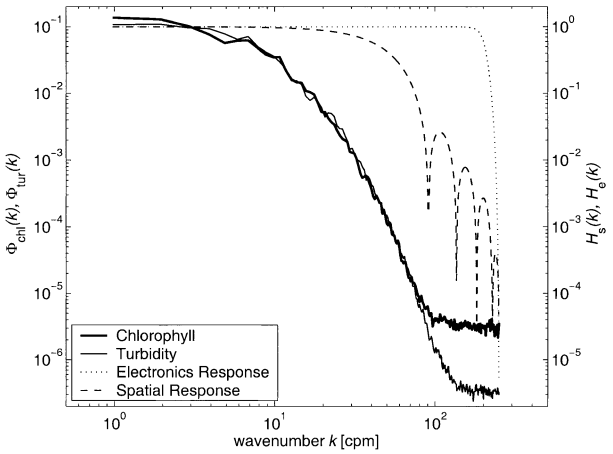

FIG. 5. Spectra of chlorophyll and turbidity and the spatial response of the chlorophyll and turbidity sensor. The spectra are nondimensionalized by dividing them by their respective total variance. Also shown is the response of the sensor's signal conditioning $H_s(k)$ and the electronics $H_e(k)$.

on the circumference of the LED circle, and its receiver beam is focused on the point of convergence of the excitation beams. The backscatter receiver has the same optical bandpass as the excitation light to ensure that fluorescent activity is not mistaken as turbid backscatter.

The sensitivity, linearity, and dynamic range of the chlorophyll sensor in response to naturally occurring fluorescence sources were determined in laboratory experiments by recording the probe output for various concentrations of natural chlorophyll solutions (pure chlorophyll-*a* and natural phytoplankton species) and sodium fluorescein (Wolk et al. 2001). As a result of the sensor geometry, the sampling volume of the probe is determined by (i) the spatial resolution in the tangential direction relative to the LED plane, and (ii) the probe's sensitivity as a function of normal distance from the LED plane. The latter was found to decrease exponentially with distance from the probe and to reach zero at $r \approx 85$ mm in clear water; 90% of the signal contribution come from the first 24 mm in front of the probe. When mounted on TurboMAP, water moves past the chlorophyll probe tangentially (i.e., the probe looks sideways), and thus the spatial resolution in the tangential direction ultimately determines the smallest resolved scales. The laboratory tests (Wolk et al. 2001) show that the probe distinguishes 2 fluorescent sources moving past the probe when the sources are separated by 20 mm or more. Sources separated by less than 20 mm are perceived as one. A simple model for the probe response is a moving average filter with a window width of 20 mm and a cosine weighting function. The wavenumber response function corresponding to such a filter is shown in Fig. 5 (heavy dashed line). Temporal smoothing by the circuit response and the sampling rate limit the maximum fall speed to 1.0 m s^{-1}.

3. Laboratory experiment

A direct comparison between the TurboMAP microstructure profiler and an acoustic Doppler velocimeter (hereafter ADV) was carried out in a open-channel flume at the Tokyo University of Fisheries on 13 December 1999. Both instruments were deployed in the flume and simultaneous measurements were undertaken at flow velocities ranging from 0.3 to 0.7 m s^{-1}. As shown by Voulgaris and Trowbridge (1998, hereafter VT98), the ADV is capable of measuring mean velocities and Reynolds stresses with an accuracy of 1%. In particular, VT98 showed that turbulence spectra computed from ADV data agree with theoretical predictions. These results enable us to evaluate the performance of TurboMAP in a controlled environment and to compare the performance of both systems under laboratory conditions.

a. Background

Following the description of homogeneous turbulence by Batchelor (1953), the three-dimensional energy spectral density of high–Reynolds number turbulence is defined as

$$\int_0^\infty E(\kappa)\, d\kappa = \frac{1}{2}\overline{(u_1^2 + u_2^2 + u_3^2)}, \qquad (5)$$

where κ is the modulus three-dimensional wavenumber vector, $\boldsymbol{\kappa}$, and u_1, u_2, u_3 are the turbulent velocity fluctuations; the subscript 1 denotes the alongstream direction. The overbar denotes the spatial average. If the turbulent field is isotropic, the form of $E(\tilde{k})$ depends only on the streamwise wavenumber component $\tilde{k}$, the viscosity ν, and the viscous dissipation rate ϵ (Kolmogorov 1941):

$$E(\tilde{k}) = \alpha\epsilon^{2/3}\tilde{k}^{-5/3}, \quad (6)$$

where $\alpha = 1.5$ is an empirical constant. The symbol $\tilde{k}$ is used to denote the radian wavenumber.

It can be shown (Tennekes and Lumley 1972) that the longitudinal and transverse velocity spectra in the inertial subrange scale as

$$\phi_{11}(\tilde{k}) = \frac{18}{55}\alpha\epsilon^{2/3}\tilde{k}^{-5/3} \quad (7)$$

$$\phi_{ii}(\tilde{k}) = \frac{4}{3}\phi_{11}(\tilde{k}), \qquad i = 2, 3. \quad (8)$$

With our experimental setup, we are able to directly determine the transverse spectra $\phi_{22}(\tilde{k})$ and $\phi_{33}(\tilde{k})$ from the velocity fluctuations u_2 and u_3 measured by the ADV. Furthermore, following scaling arguments,

$$\epsilon \sim \boldsymbol{u}^3/\boldsymbol{L}, \quad (9)$$

where $\boldsymbol{L}$ is the energy containing length scale and $\boldsymbol{u}$ is the characteristic velocity (or scale velocity) of the turbulent flow. Here, $\boldsymbol{L}$ is determined by the size of the turbulence-generating grid in the flow tank, and the velocity scale $\boldsymbol{u}$ is given by the measured root-mean-square (rms) velocity fluctuations. The scale constant that turns (9) into an equality ranges from 0.8 to 1.4 (Batchelor 1953, his Fig. 6.1). A value of 1 brings the theoretical spectral levels (8) into agreement with the measured levels and verifies that the turbulence intensity is reasonably consistent with expectations. The important issue is the agreement between the shear probe and ADV, both of which measure velocity fluctuations but operate on completely different physical principles.

The dissipation shear spectrum measured by TurboMAP is $\psi_{33}(\tilde{k})$ [or $\psi_{22}(\tilde{k})$, depending on the orientation of the shear probe in the flow tank] and is given by

$$\int_0^\infty \psi_{33}(\tilde{k})\, d\tilde{k} = \overline{\left(\frac{\partial u_3}{\partial x_1}\right)^2}. \quad (10)$$

The shear spectrum can be turned into a velocity spectrum through division by $\tilde{k}^2$,

$$\phi_{33}(\tilde{k}) = \tilde{k}^{-2}\psi_{33}(\tilde{k}). \quad (11)$$

Thus, the shear spectrum measured by TurboMAP can be compared to the corresponding velocity spectrum measured by the ADV.

b. Acoustic Doppler velocimeter

The ADV unit used in the test is manufactured by Nortek AS, model ADVLab. The operating principle is outlined here only briefly, and details can be found in, for example, Lohrmann et al. (1994). The instrument infers flow velocities by transmitting a 10-MHz acoustic pulse and measuring the Doppler-shifted frequency along three distinct spatial axes. The sensor consists of one transmit transducer and three receive transducers. All transducers are arranged in one plane, and the receivers are spaced at 120° azimuthal angles around the transmitter. The acoustic beams of the receivers are oriented so that they intercept the transmit beam 50 mm below the transducer plane. This intersection creates a popcorn-shaped sampling volume that is approximately 9 mm long and 6 mm in diameter (K. Horn 2000, personal communication). Depending on the operating conditions and instrument settings, the ADV takes 200 instantaneous velocity readings (pings) per second for each axis and averages these pings to improve the measurement statistics. In this experiment, the instrument is set to produce 100 velocity readings per second (100-Hz sampling rate), which means that each recorded sample is the average of two pings.

To improve the signal-to-noise ratio during the experimental runs, 250 g of seeding material are added to the water in the flow tank. The seeding material is supplied by Nortek and consists of neutrally buoyant, hollow glass spheres of approximately 10-μm diameter. With this treatment, the correlation coefficient between transmit and receive pulses is $\geq$0.8 at all times, which exceeds the minimum value of 0.7 suggested for accurate measurements (Nortek 1998).

Due to the geometry of the sensor head, noise along the measurement beams is enhanced approximately by a factor of 11 for the horizontal velocity components and approximately by 0.35 for the vertical component (VT98). For our experiment, the ratio of noise levels $\sigma_{u,v}^2/\sigma_w^2 \approx 33$ for still water and flow speeds up to 0.3 m s^{-1}, which is consistent with VT98. For higher speeds, this noise ratio decreases as the correlation coefficient decreases.

In the following, velocities measured by the ADV are denoted with the symbols $\tilde{u}$, $\tilde{v}$, and $\tilde{w}$, and their averages are

$$U = \overline{\tilde{u}}, \qquad V = \overline{\tilde{v}}, \qquad W = \overline{\tilde{w}}, \quad (12)$$

where the average is computed over 120-s records during which the downstream velocity in the flume is held constant. The averaging time is much longer than the large eddy turnover timescale $\boldsymbol{D}/\boldsymbol{u} \sim 1/0.05 = 20$ s, where $\boldsymbol{D}$ represents the typical dimension of the flow tank and $\boldsymbol{u}$ the characteristic turbulent velocity (see the next section for details). Instantaneous turbulent velocity fluctuations are given by

$$u = \tilde{u} - U, \qquad v = \tilde{v} - V, \qquad w = \tilde{w} - W. \quad (13)$$

c. Experimental setup and procedure

The flume dimensions are 10 m $\times$ 1.45 m $\times$ 1.2 m (length $\times$ width $\times$ water depth) and downstream flow speeds of up to 0.7 m s^{-1} can be achieved. The water temperature in the flume at the beginning of the experiment is 11°C, but no attempts are made to maintain this temperature throughout the test. To produce a highly energetic turbulent flow, a grid as shown in Fig. 6 is

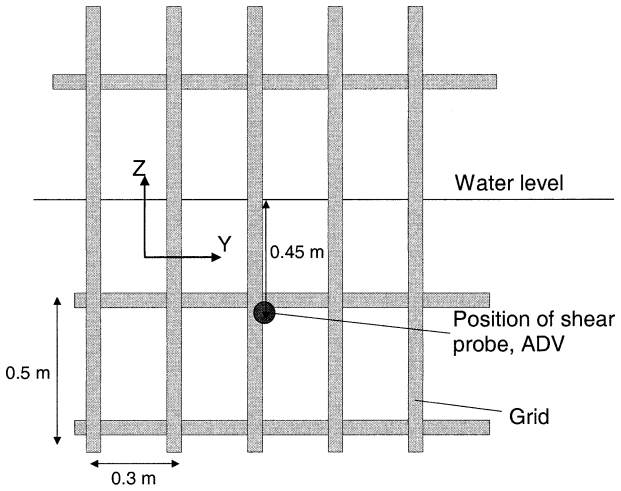

FIG. 6. Experimental setup in the flume (looking downstream). The position of the shear probe and the ADV sampling volume is indicated by the marker. The grid is 1.45 m upstream of the shear probe.

placed 1.45 m upstream of the shear probe. The grid is constructed from brass pipes with a diameter of 50 mm. Here, 5 pipes are spaced at 0.3 m intervals in the y direction and 2 pipes at 0.5 m in the z direction.

Five experimental runs are carried out with grid and 5 runs without grid at nominal downstream flow speeds of $\boldsymbol{U} = 0.3$, 0.4, 0.5, 0.6, and 0.7 m s^{-1}. During each run, data records are collected for 120 s. The run with grid and $\boldsymbol{U} = 0.7$ m s^{-1} is excluded from the analysis, because in this run the signal levels exceed the dynamic range of TurboMAP's shear probe circuit.

The ADV sensor head is connected rigidly to the tank superstructure by a 15-mm-diameter steel rod, and the sensor head is oriented so that u is positive upstream and w is positive upward. The ADV sensor head is 400 mm below the water surface, and the sampling volume is level with the position of the shear probe. Because of mechanical constraints, the sampling volume is located 150 mm upstream of the shear probe.

The TurboMAP profiler is placed horizontally into the flow tank so that the sensor nose points into the flow. The instrument is suspended from the tank's superstructure with two Kevlar wires (2-mm diameter), which are attached to TurboMAP's dropoff weights. The wires are faired by contiguously applying 50-mm-wide strips of adhesive tape, in order to reduce strumming of the these wires. The rear of the instrument is attached rigidly to the tank superstructure by a 50-mm-diameter brass pipe. The rigid connection prevents heaving and pitching motions of the instrument, which occur when the instrument is pushed downstream by the oncoming flow.

The shear probe is sensitive to only one cross-stream component of the flow, in this case v or w. Since, the ADV's noise level is lowest for the w component, we seek to align the shear probe with that axis. Due to the experimental setup, there is some ambiguity in the relative alignment of the shear probe with respect to the ADV's coordinate system, so the alignment is determined as follows. The shear probe signal is numerically integrated to make it proportional to velocity, that is,

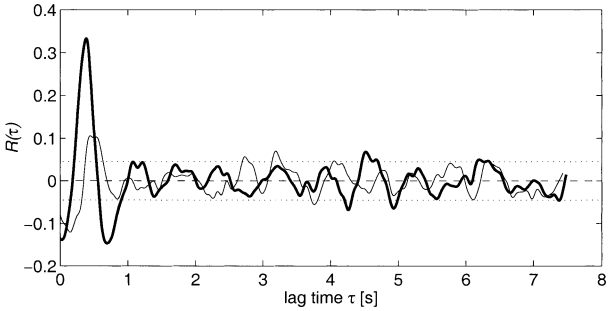

FIG. 7. Lagged cross-correlation function $R(\tau)$ between the integrated shear probe signal, w_s, and the cross-stream velocities w and v measured by the ADV (thin line and heavy line, respectively), for $\boldsymbol{U} = 0.4$ m s^{-1}.

$$w_s = \int \frac{\partial w}{\partial t}\, dt. \tag{14}$$

Here, $\partial w/\partial t$ is the recorded shear probe signal, where the symbol w_s is used to denote either of the two cross-stream velocity components, w_s or v_s. The integrated signal w_s is then compared to the cross-stream velocities v, w of the ADV. Figure 7 shows the lagged cross-correlation function $R_{sw}(\tau)$ between w_s and w (heavy line) and $R_{sv}(\tau)$ between w_s and v (thin line) for the run with $\boldsymbol{U} = 0.4$ m s^{-1}. To match the noise levels of the respective signals, the w_s, v, and w signals are low-pass filtered at 10 Hz before calculating the cross-correlation functions. The short-dashed line at ± 0.045 is the 95% confidence interval of the sample distribution of $R_{sw}(\tau \geq \tau_0)$, where $\tau_0 = 1$ s is the decorrelation time of the two series (Lueck and Wolk 1999). This line represents the correlation of two random time series that have the same statistical properties as w_s and w. The lag-time τ can be interpreted as the time it takes an eddy to travel downstream from the ADV to the shear probe. At $\tau = 0.38$ s there is a significant correlation between w_s and w of $R_{sw}(\tau) = 0.33$, while $R_{sv}(\tau) = 0.062$. Since both correlation coefficients exceed the 95% confidence interval, we conclude that the shear probe's sensitive axis is not entirely aligned with the vertical axis of the ADV coordinate system. From the correlation coefficients, we estimate the angle α between the ADV z axis and the sensitive axis of the shear probe from $\cos\alpha = R_{sw}(\tau)/[R_{sv}^2(\tau) + R_{sw}^2(\tau)]^{1/2}$ for $\tau = 0.38$, which gives $\alpha \approx 11°$.

The existence of a statistically significant value of R_{sw} shows that the shear probe signal and the ADV w component are coherent. However, because of the spatial separation of the probes in the downstream direction, this coherence vanishes at higher wavenumbers, as shown in Fig. 8. The heavy line is the coherency spectrum between the integrated shear probe signal w_s and the w component of the ADV for a run with $\boldsymbol{U} = 0.4$

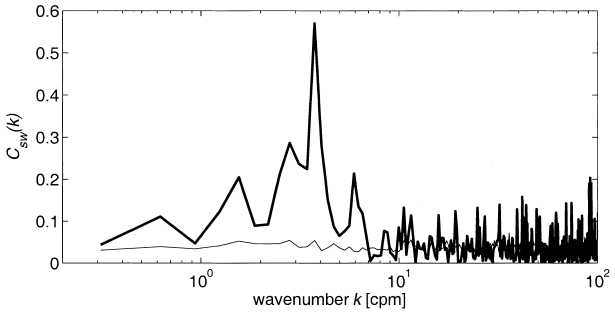

FIG. 8. Coherence spectrum for w_s and w for $\boldsymbol{U} = 0.4$ m s^{-1}. The thin line is the coherence spectrum of two uncorrelated series with the same statistical properties as w_s and w.

m s^{-1}. The light line is the coherence spectrum of two uncorrelated time series, which are constructed from w_s and w using a ''Monte Carlo'' method. The ADV and shear probe signals are coherent at low wavenumbers. At $k_0 = 7$ cpm the coherence falls below the significance level, and the corresponding length scale k_0^{-1} is consistent with the spatial separation of the two probes of 0.15 m. Even though the signals from the ADV and the shear probe are not coherent for wavenumbers higher than k_0, we can still compare them in a statistical sense. The instruments will not be able to measure identical turbulent eddies, but since the distance to the source of the turbulence is 10 times larger than the distance between the probes, we do not expect significant changes in the statistical properties of the flow over the separation distance of the probes.

d. Flow characteristics

Table 2 summarizes the flow regime in the flume during the experimental run with the grid. Here σ_u, σ_v, σ_w are the rms of the turbulent velocity fluctuations defined in (13). They reveal a slight asymmetry in the flow, which is caused by an asymmetry in the experimental setup and by secondary circulation effects in the flume. As indicated in Fig. 6, the location of the sensors is not perfectly aligned with the node of the grid. Most of the asymmetry is contained in the energy containing scales of the flow and does not influence the statistics of the inertial subrange measurements.

The ϵ values listed in Table 2 are computed from the scale relation (9) with $\boldsymbol{L} = 0.05$ m given by the diameter of the grid pipes and

$$\boldsymbol{u}^2 = 1/3\overline{(u^2 + v^2 + w^2)} \tag{15}$$

(Tennekes and Lumley 1972). The Reynolds numbers $\mathrm{Re} = \boldsymbol{UL}/\nu$, where $\boldsymbol{U}$ is the nominal flow velocity, exceed 15 000 for all runs and are sufficiently large to ensure turbulent flow.

e. Results and discussion

The results of the experimental runs with grid are summarized by considering the transverse velocity spectra $\phi_{vv}(k)$, $\phi_{ww}(k)$ computed from the ADV and the shear probe data. For the experimental runs with grid and for nominal downstream flow speeds of $\boldsymbol{U} = 0.3$, 0.4, 0.5, and 0.6 m s^{-1}, average spectra are computed as follows. For each flow speed, one frequency spectrum is computed from the 120-s record of v, w, and $\partial w/\partial x$ using Welch's averaged periodogram method (e.g., Oppenheim and Schafer 1999) with a fast Fourier transform (FFT) window length of 4 s and a cosine window function for each FFT window. Frequency spectra are turned into wavenumber spectra by multiplying them by the average downstream velocity U as in (4). The shear spectra $\psi_{ww}(k)$, computed from the shear probe signal, are converted to velocity spectra using (11). Note that throughout this paper, measured spectra are expressed in terms of the cyclic wavenumber $k = \tilde{k}/2\pi$, which has units of cycles per meter (cpm).

Spectra for the runs with grid and $\boldsymbol{U} = 0.3$ and 0.5 m s^{-2} are plotted in Fig. 9. The spectra for the runs with $\boldsymbol{U} = 0.4$ and 0.6 m s^{-1} exhibit the same characteristics as the ones shown. The ADV v and w components are shown as triangles and squares, respectively, and the shear probe spectrum is shown as circles. The straight line is the scaled $-5/3$ curve predicted by (8), where the scaling factor ϵ is estimated from the measured spectrum by evaluating (6) at $k = 10$ cpm. For the spectra shown, the estimates are $\epsilon = 1.5 \times 10^{-3}$ and 5.5×10^{-3} W kg^{-1} for $\boldsymbol{U} = 0.3$ and 0.5 m s^{-1}, respectively. These values agree within a factor of unity with the ϵ values computed from the scale relation (9), listed in Table 2.

Within their confidence intervals, the velocity spectra of the ADV w component and the shear probe show

TABLE 2. Ancillary data from the flume experiment with grid. Here $\boldsymbol{U}$ is the nominal downstream flow velocity; U, V, W are the measured mean velocitites; σ_u, σ_v, σ_w are the rms velocity fluctuations; $\boldsymbol{u}$ is the characteristic velocity scale defined by (15); $\epsilon = \boldsymbol{u}^3/\boldsymbol{L}$ is the dissipation rate with $\boldsymbol{L} = 0.05$ m; and Re is the Reynolds number.

$\boldsymbol{U}$	U	V	W	σ_u	σ_v	σ_w	$\boldsymbol{u}$	$\epsilon = \boldsymbol{u}^3/\boldsymbol{L}$	Re
m s^{-1}	cm s^{-1}			cm s^{-1}			cm s^{-1}	10^{-3} W kg^{-1}	
0.3	−30.71	0.18	−0.52	4.88	4.68	3.25	4.33	1.62	15 300
0.4	−40.19	0.11	−0.24	6.10	5.77	4.10	5.39	3.14	20 000
0.5	−47.62	0.13	−0.36	6.70	6.36	4.79	6.01	4.34	25 000
0.6	−59.19	0.46	−0.88	8.45	7.66	6.02	7.45	8.26	30 000
0.7	−67.94	0.06	−1.01	10.1	9.29	7.04	8.92	14.2	35 000

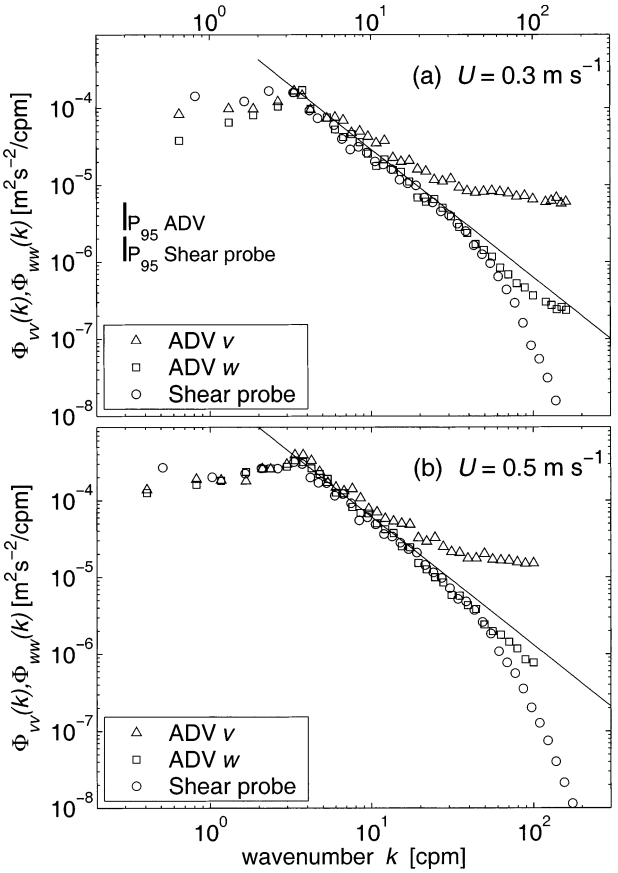

FIG. 9. For the experimental run with grid, transverse wavenumber spectra $\phi_{vv}(k)$ and $\phi_{ww}(k)$ from the ADV, and $\phi_{ww}(k)$ from TurboMAP. Downstream nominal flow speeds are as indicated in (a) and (b). The solid straight lines are the theoretical transverse Kolmogorov spectrum given by (8). Vertical bars labeled P_{95} are the 95% confidence intervals of the spectra (Jenkins and Watts 1968, their section 6.4.3). The viscous dissipation wavenumbers for both cases are above 1000 cpm.

excellent agreement over approximately two decades in wavenumber space. Above 1 cpm all spectra slope upward until they reach a turning point at around 3.5 cpm, after which the spectra follow a $-5/3$ slope. The location of the turning point is consistent with theoretical considerations, which predict the $-5/3$ part of the spectrum to begin at $\tilde{k}\boldsymbol{L} \simeq 1.8$ (Tennekes and Lumley 1972).

Starting at 4 cpm, both the shear probe spectrum and the ADV w spectrum follow the theoretical $-5/3$ slope predicted by Kolmogorov for well over 1 decade in wavenumber space. Both spectra break from the $-5/3$ slope at around 40 cpm. This point is determined by the size of the sensors in the alongstream direction. Both sensors have approximately the same dimension in the x direction, and so their spectra are congruent up to the spatial cutoff wavenumber.

Around 100 cpm, the ADV spectrum curves slightly upward as it approaches the noise floor of this instrument. This causes the ADV spectrum to roll off slightly slower than the shear probe spectrum. The horizontal

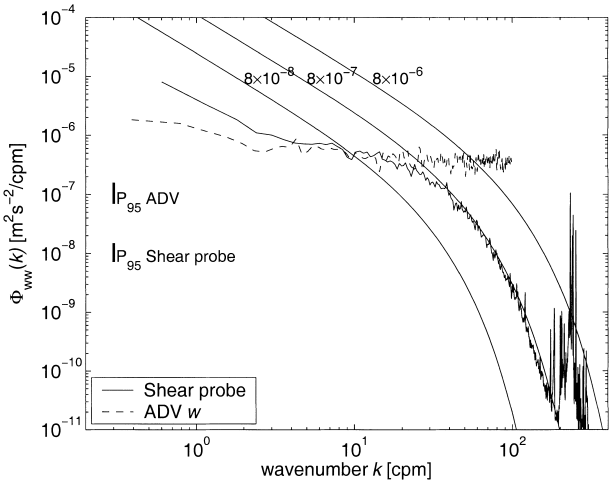

FIG. 10. Transverse velocity spectra $\phi_{ww}(k)$ measured by the TurboMAP and the ADV for the run without grid and $\boldsymbol{U} = 0.7$ m s^{-1}. The smooth curves are the Panchev–Kesich spectra corresponding to indicated dissipation rates.

components of the ADV are noisier than the vertical component, so the v spectrum does not follow the theoretical curve well. It already breaks from the $-5/3$ slope at 7 cpm.

Evidently, in the wavenumber range unaffected by averaging effects, the vertical flow component is consistently measured by both measurement systems. For this highly energetic flow regime, the vertical component of the ADV and the shear probe both resolve the inertial subrange of the turbulent flow over approximately one decade in wavenumber space. Even though this agreement is encouraging, the measurement objective is to resolve the dissipation range of oceanic turbulence. The turbulence levels produced in the experimental runs with grid are extremely high for oceanic conditions. Even for the slowest downstream velocity of 0.3 m s^{-1}, the dissipation rate estimated from (9) is of $O(10^{-3})$ W kg^{-1}, which is an extreme value for open-ocean conditions.

To gauge the performance of both measurement systems at turbulence levels closer to the oceanic range, experimental runs are conducted without grid. Shown in Fig. 10 are the transverse spectra $\phi_{ww}(k)$ measured by the ADV and the shear probe for $\boldsymbol{U} = 0.7$ m s^{-1}. The shear probe spectrum is boosted by the response function (3) with $k_c = 50$ cpm. Most of the ADV spectrum is saturated with noise and only at the lowest wavenumbers, below 2 cpm, does the spectrum rise above the noise floor. On the other hand, the shear probe spectrum continues to decrease without reaching a noise floor. At around 150 cpm, the spectrum shows the onset of vibration noise, caused by the strumming of the suspension wires in the flow. The Panchev–Kesich turbulence spectrum (Panchev and Kesich 1969) represents an extension to Kolmogorov's turbulence theory. Therefore, we compare the spectra measured in the laboratory

to the Panchev–Kesich form. [The field data presented in the next section will be compared to the empirical Nasmyth form (Nasmyth 1970).] The smooth curves in Fig. 10 are the theoretical turbulence spectra scaled for dissipation rates of $\epsilon = 8 \times 10^{-8}$, 8×10^{-7}, and 8×10^{-6} W kg^{-1}. At low wavenumbers, the measured spectra are not expected to follow the Panchev–Kesich spectrum. In this run, the turbulence in the tank is not generated by the grid, and so there is little excitation of the low wavenumbers of the turbulent spectrum. The lack of sufficient scale separation between the energy containing scales and the dissipation scales prevents the development of an inertial subrange. However, between 40 and 100 cpm (the dissipation range), the response-corrected spectrum shows a remarkable agreement with the theoretical spectrum. Above 100 cpm the shear probe spectrum is slightly below the theoretical curve.

4. Field test

Datasets recorded during several deployments of TurboMAP in coastal and offshore waters around Japan are presented in the following sections. The first dataset exhibits the performance of the instrument in general, the second dataset gives an indication of the noise levels in terms of dissipation rate ϵ, and the third dataset highlights the bio-optical sensors.

a. Measurements near an isolated island

Figure 11 shows depth profiles of all channels recorded near Mikura Island, approximately 100 miles south of Tokyo Bay. The data are taken in the Kuroshio, downstream of the island. The water column in this area is highly oligotrophic, so the chlorophyll and turbidity signals of this profile show only weak variability. The temperature and conductivity signals indicate the presence of the stable density gradient between 120 and 145 m. Both signals show a steplike structure resulting from the turbulent mixing processes working to reduce the mean vertical gradients. The conductivity signal reveals a fine structure with numerous overturns. Above 120 m depth, the shear signal $\partial u/\partial z$ shows variations with peak-levels around 0.05 s^{-1}, corresponding to dissipation rates of about $\epsilon = 10^{-8}$ W kg^{-1}. The velocity shear increases below 120 m to peak values of $\sim$1 s^{-1}, corresponding to dissipation rates around 6×10^{-6} W kg^{-1}. The increase in velocity shear is accompanied by significant temperature gradients, which have their largest excursions just above and below the local mixing regions of the step structure.

The low-frequency portions of the accelerometer signals indicate the tilt angle of the instrument. Throughout the depth profile, the profiler performs slow pendulum motions. These motions do not interfere with the shear measurements, since their frequencies are below 0.5 Hz and, thus, does not enter the wavenumber band of the shear spectrum. As the profiler enters the highly turbulent layer, the amplitude of the pendulum motions increases by approximately a factor of 2 due to the increased large-scale shear in this region. The profiler's maximum tilt angle off the vertical is approximately 2°.

Dissipation spectra $\psi(k)$ computed from the shear signal in Fig. 11 are shown in Fig. 12 along with the corresponding scaled Nasmyth universal spectra. The upper curve is from $127 \leq z \leq 135$ m. The lower curve is from $105 \leq z \leq 115$ m. The spectra are computed using Welch's averaged periodogram method described in section 3e with an FFT length of 2 s. The rate of change of the profiler sinking velocity over this time interval is negligible. The dissipation rates ϵ based on the measured spectra are $\epsilon = 4.0 \times 10^{-6}$ W kg^{-1} ($127 \leq z \leq 135$ m) and $\epsilon = 1.4 \times 10^{-7}$ W kg^{-1} ($105 \leq z \leq 115$ m), and they are computed by integrating the measured shear spectrum

$$\epsilon = \frac{15}{2}\nu\overline{\left(\frac{\partial u}{\partial z}\right)^2} = \frac{15}{2}\nu\int_{k_1}^{k_2}\psi(k)\,dk, \qquad (16)$$

where ν is the kinematic viscosity and the overbar denotes the spatial average. The lower integration limit, k_1 is set to 1 cpm and the upper limit, k_2, is the highest wavenumber not contaminated by vibration noise (200 and 100 cpm, respectively, for the upper and lower spectrum). Before integration, the spectra are boosted by the response function (3) to compensate for signal attenuation due to averaging effects. The narrowbanded spikes around 150 and 225 cpm are the result of vibrations, which are discussed in more detail in the following section. The 95% confidence interval of the spectral estimators is shown as the vertical bar (Jenkins and Watts 1968, their section 6.4.3). Any systematic errors associated with, for example, the measurement of the instruments sinking velocity or calibration of the shear sensor, would shift the measured spectra along a line parallel to the ordinate axis. The measured spectra might still have the ''right shape'' but they would not overlap with the Nasmyth spectrum. Random measurement errors introduced in the shear signal via errors in the sinking velocity or by characteristics of the electronics would result in a distortion of the spectra so that their shapes would differ from the expected empirical curve. After correction for the spatial averaging of the shear probe, the measured spectra agree well with the universal spectrum in both shape and magnitude for all wavenumbers up to the viscous cutoff.

b. Dissipation noise levels

Figure 13 shows a dissipation spectrum of a quiescent shear signal collected in the off-shelf region in the Japan Sea between 315- and 322-m depth. The TurboMAP unit used in this deployment had a protective guard cage at the front and a flotation collar at the back to compensate the extra weight of the cage. The dissipation rate for the spectrum shown is $\epsilon = 4.9 \times 10^{-10}$ W kg^{-1}

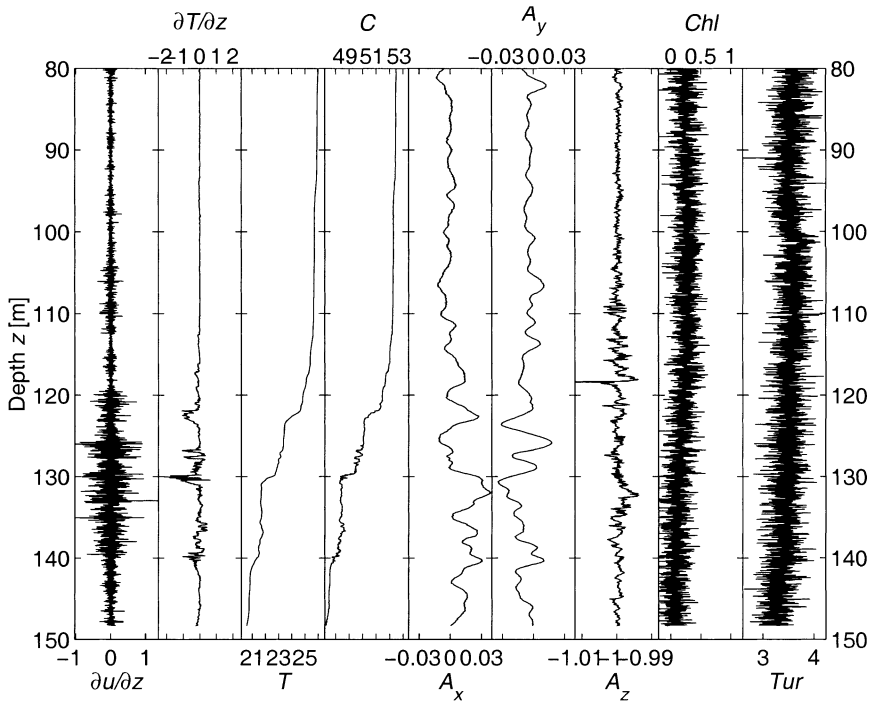

FIG. 11. Depth profiles of shear $\partial u/\partial z$ (s^{-1}); temperature gradient $\partial T/\partial z$ (K m^{-1}); temperature T (°C); conductivity C (mmho m^{-1}); body accelerations Ax, Ay, Az (G); chlorophyll Chl (μg L^{-1}); and turbidity Tur (ppm).

and is computed as described above with an FFT window length of 4 s. The smooth curves are the universal spectra for dissipation rates ranging from 1×10^{-10} to 1×10^{-5} W kg^{-1}.

Evident in the shear spectrum are a number of noise spikes. The broadbanded noise between 15 and 70 cpm is probably caused by the brushes at the back of the instrument (cf. Fig. 1a). The two sharp peaks at 105 and 210 cpm (harmonic) have frequencies corresponding to the first bending mode of the pressure case (Miller et al. 1989). The presence of these noise sources influences

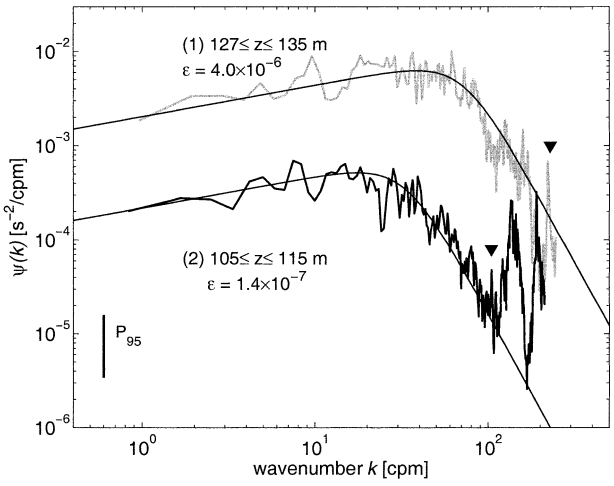

FIG. 12. Dissipation spectra and their corresponding universal spectra for two depth regions of the shear signal shown in Fig. 11 [(1) $127 \le z \le 135$ m, (2) $105 \le z \le 115$ m]. Both spectra are corrected for the spatial averaging of the shear probe. The dissipation rates ϵ are computed from the integrals of the measured spectra. The inverted triangles mark the viscous dissipation wavenumber. The vertical bar is the 95% confidence interval of the upper spectrum.

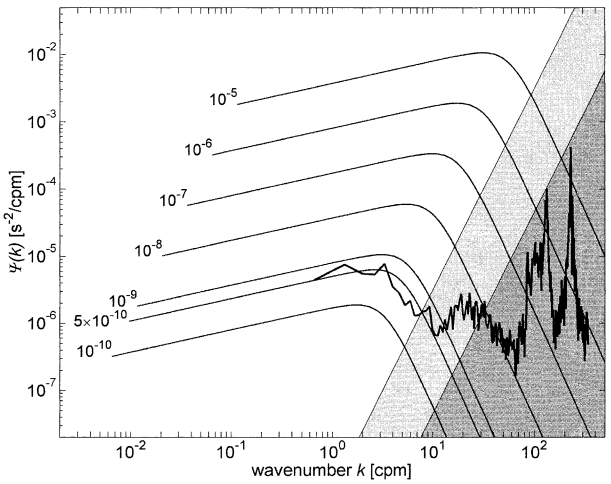

FIG. 13. Dissipation spectrum of a quiescent section of data between 315- and 322-m depth. The smooth curves are the universal spectra for various dissipation rates. The slanted line delimiting the dark shaded region is the viscous dissipation wavenumber k_ν as a function dissipation rate ϵ. The line delimiting the light-shaded region corresponds to $0.5k_\nu$.

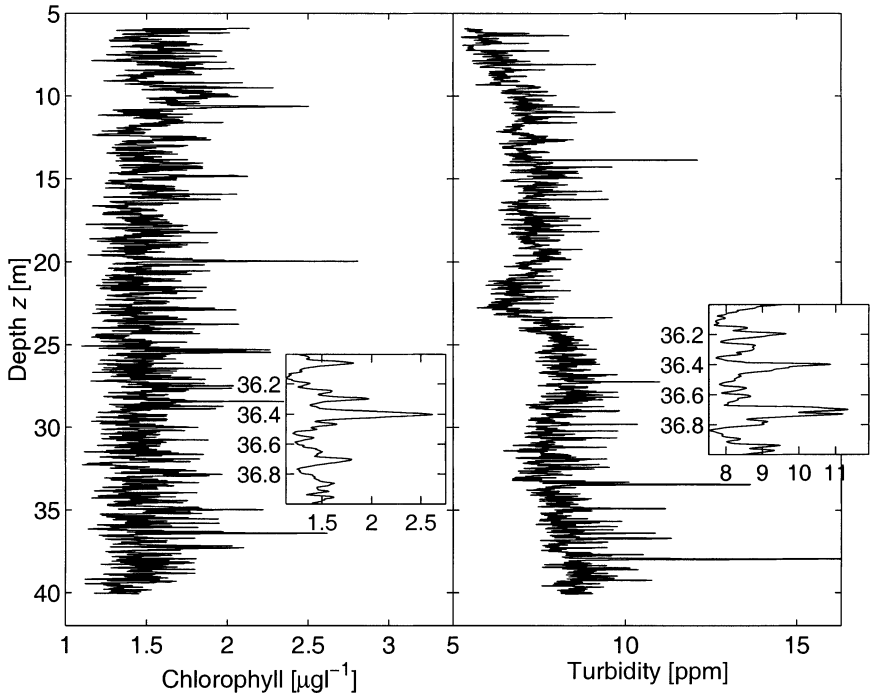

FIG. 14. Depth profiles of chlorophyll and turbidity. The insets show enlarged sections of the respective signals.

the dissipation measurements only at very low turbulence levels, and even at these levels it is possible to infer the correct dissipation rate from the measured spectra.

The highest wavenumber of interest in the dissipation spectra is the viscous dissipation wavenumber (or Kolmogorov wavenumber):

$$k_\nu = \frac{1}{2\pi}\left(\frac{\epsilon}{\nu^3}\right)^{1/4} \quad \text{(cpm)}. \tag{17}$$

In Fig. 13, k_ν is drawn as a function of dissipation rate as the slanted line that delimits the dark-shaded region. The point where a given universal spectrum enters the dark shading is the wavenumber at which 97% of its energy is captured. The vibration peaks of the measured spectrum at 105 and 210 cpm lie in the dark-shaded region; therefore, they do not bias the measurements. On the other hand, for turbulence levels between 5×10^{-10} and 1×10^{-8} W kg^{-1}, the broadband noise between 15 and 70 cpm can bias the integral of the measured spectrum because the noise hump rises above spectral levels before k_ν is reached.

The dissipation rate can still be inferred from the measured spectrum by truncating the integration at $0.5k_\nu$ and extrapolating the spectrum based on the shape of the empirical spectrum. The light-shaded area in Fig. 13 is the region $k > 0.5k_\nu$. About 87% of the turbulent energy is contained at wavenumbers below $0.5k_\nu$, and so the truncated integration yields a reasonable approximation of the dissipation rate. (This detail is briefly discussed in the appendix.) With the approximated dissipation rate, the empirical spectrum can be scaled, and the remaining variance above $0.5k_\nu$ can be recovered by iteration (Moum et al. 1995).

In Fig. 12, the triangular markers show the locations of k_ν for the respective spectra. We notice that for the spectrum from the highly turbulent regions, (1), the vibration peak is just below the viscous dissipation wavenumber. The reason for this is that the vibrations are a frequency response of the system. Thus, when spectra are converted to wavenumbers using (4), the vibration peaks fall onto different wavenumbers, depending on the sinking velocity of the instrument. For the data shown in Fig. 12, the sinking velocity is 0.52 m s^{-1} compared to 0.43 m s^{-1} in Fig. 13.

c. Measurements in a tidal channel

The depth profiles from a tidal channel in the Seto Inland Sea show a significant amount of variability in the chlorophyll and turbidity signals (Fig. 14). The large excursions of the chlorophyll signal at, for example, 20 and 36 m have half-widths of approximately 50 mm. The widths of the excursions are evident in high-resolution plots of the signals. The excursions are thus within the spatial resolution of the chlorophyll/turbidity sensor and are caused by encounters with local patches of fluorescent material.

The autospectra of both signals are shown in Fig. 5, where each spectrum is normalized by its own variance.

The noise level of the sensor is indicated by the flat region of the spectra above 100 cpm. Below 100 cpm, the signals are well above the noise, and chlorophyll and turbidity signals are larger by factors of about 10^4 and 10^5, respectively, than the noise level. Above 10 cpm, the turbidity and chlorophyll spectra roll off with increasing wavenumber. The rolloff is steeper than the response function of the probe (shown as the dashed line), which proves that the rolloff must be a real phenomenon and not an artifact of the spatial averaging of the probe.

5. Summary

Data from laboratory and field tests were evaluated to gauge the performance of the free-falling profiler TurboMAP, designed to simultaneously measure physical and biological microstructure. A direct comparison between TurboMAP and an acoustic Doppler velocimeter was carried out in a flume, in which a highly energetic grid turbulence was created. Velocity spectra from both instruments agree over 2 decades in wavenumber space and are coherent up to 7 cpm.

Noise level estimates in terms of the dissipation rate ϵ showed that TurboMAP resolves rates as low as 5×10^{-10} W kg^{-1}. Lower values of ϵ can be inferred by comparing the measured spectra against the assumed universal form.

Field data from TurboMAP's chlorophyll and turbidity sensors revealed a centimeter-scale structure in fluorescence and suspended particle distributions. Spectra of these signals proved to be unaffected by spatial averaging of the sensor and rise well above the noise floor of the sensor.

Acknowledgments. We thank Kou Matsuda for allowing us to use the flume facility at the Tokyo University of Fisheries; Takeshi Matsuno of Kyushu University for offering the dataset to Fig. 13; as well as Toshihiro Yazu for his help in operating TurboMAP during the experiments. Thanks also to Ketil Horn and Atle Lohrman of Nortek AS for the helpful discussions regarding the acoustic Doppler velocimeter. R. G. Lueck is supported by the Office of Naval Research under Grant N00014-93-1-0362. The development of TurboMAP was funded in parts by the Monbu-Sho Science and Research Aid (Grant Kiban C2 10640421) and Alec Electronics Co., Ltd.

APPENDIX

Nasmyth's Spectrum

Measured oceanic turbulence spectra are routinely compared to the empirical turbulence spectrum, which was measured by Nasmyth (1970). Oakey (1982) tabulated the values of the so-called Nasmyth spectrum, and these points are shown as asterisks in Fig. A1. Note

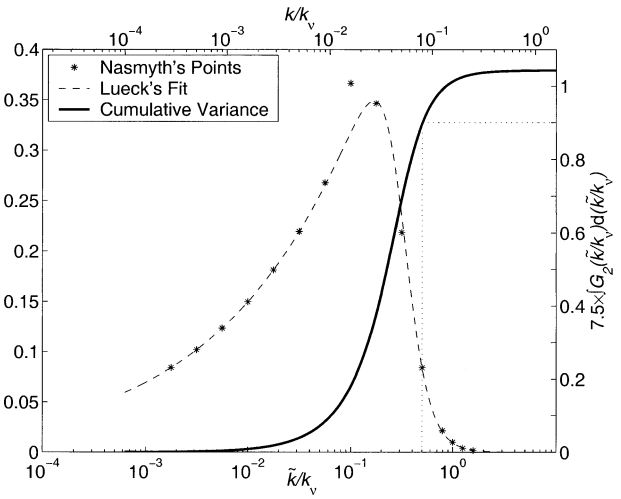

FIG. A1. The Nasmyth empirical spectrum as tabulated by Oakey (1982), shown as *. The solid line is the cumulative variance of the fitted curve given by (A1).

that the G_2 values given by Oakey (1982) are in terms of k/k_ν, where k is the cyclic wavenumber. Oakey's scaling is indicated by the upper tick marks of the graph. It has been pointed out by several authors (e.g., Moum et al. 1995; Gregg 1999) that there is no theoretical justification for the Nasmyth spectrum; it is merely a carefully measured dataset that was accepted by the oceanographic community as being representative of the spectral form of oceanic turbulence. A theoretically derived form of the turbulence spectrum is given by Panchev and Kesich (1969) and their form is used in Fig. 10 to compare against the spectra measured in the flow tank.

A discussion on which spectral form should be preferred is beyond the scope of this contribution. The authors of this paper routinely use the Nasmyth form to judge the shape of their measured oceanic dissipation spectra. In practice, a fitted form of the Nasmyth spectrum is used, which was suggested by R. G. Lueck (1996, personal communication):

$$G_2(k_n) = \frac{8.05k_n^{1/3}}{1 + (20k_n)^{3.7}}, \qquad \text{(A1)}$$

where $k_n = \tilde{k}/k_\nu$ is the nondimensional wavenumber and $\tilde{k}$ is the radian wavenumber. This form is shown in Fig. A1 as a dashed line, and it fits the original data well (within $\pm 5\%$) except at one point. That point was rejected by Lueck because it rises anominously above the $-1/3$ slope in the inertial subrange.

The cumulative integral of (A1) is shown as the heavy line in Fig. A1, and it integrates to a maximum value of 1.04 (the integral of the original Nasmyth points is 1.05). At $0.5k_n$ the integral is 0.9, which represents $0.9/1.04 = 0.87$ of the entire variance of the turbulence spectrum. Thus, in cases where the measured turbulence spectrum is not fully resolved—due to vibration noise

or limited bandwidth of the shear probe—a good estimate of the dissipation rate can be achieved by integrating the spectrum to $0.5k_n$ and inferring the rest of the variance from the Nasmyth (or Panchev–Kesich) spectrum.

REFERENCES

Batchelor, G. K., 1953: *The Theory of Homogeneous Turbulence.* Cambridge University Press, 197 pp.

Denman, K., and A. Gargett, 1995: Biological–physical interactions in the upper ocean: The role of vertical and small scale transport processes. *Annu. Rev. Fluid Mech.,* **27,** 225–255.

Dewey, R. K., W. R. Crawford, A. E. Gargett, and N. S. Oakey, 1987: A microstructure instrument for profiling oceanic turbulence in coastal bottom boundary layers. *J. Atmos. Oceanic Technol.,* **4,** 288–297.

Gargett, A., and J. Marra, 2002: Effects of upper-ocean physical processes—turbulence, advection, and air–sea interaction—on oceanic primary production. *The Sea*, A. R. Robinson, J. J. McCarthy, and B. J. Rothschild, Eds., Biological–Physical Interactions in the Ocean, Vol. 12, John Wiley and Sons, 19–49.

Gregg, M. C., 1999: Uncertainties and limitations in measuring ϵ and χ_T. *J. Atmos. Oceanic Technol.,* **16,** 1483–1490.

Jenkins, G. M., and D. G. Watts, 1968: *Spectral Analysis and Its Applications.* Holden-Day, 525 pp.

Kolmogorov, A. N., 1941: The local structure of turbulence in an incompressible viscous fluid for very large Reynolds number. *C. R. Acad. Sci. USSR,* **30,** 301–305.

Kørboe, T., 1997: Small-scale turbulence, marine snow formation, and planktivorous feeding. *Sci. Mar.,* **61,** 141–158.

Lohrmann, A., R. Cabrera, and N. C. Kraus, 1994: Acoustic-doppler velocimeter (ADV) for laboratory use. *Proc. Conf. on Fundamentals and Advancements in Hydraulic Measurements and Experimentation,* Buffalo, NY, American Society of Civil Engineers, 351–365.

Lueck, R. G., and F. Wolk, 1999: An efficient method for determining the significance of covariance estimates. *J. Atmos. Oceanic Technol.,* **16,** 773–775.

——, D. Huang, D. Newman, and J. Box, 1997: Turbulence measurements with an autonomous moored instrument. *J. Atmos. Oceanic Technol.,* **14,** 143–161.

Macoun, P., and R. Lueck, 2002: Modeling the spatial response of the airfoil shear probe using different sized probes. *J. Atmos. Oceanic Technol.,* submitted.

Miller, J. B., M. C. Gregg, V. W. Miller, and G. L. Welch, 1989: Vibration of tethered microstructure profilers. *J. Atmos. Oceanic Technol.,* **6,** 980–984.

Moum, J. N., M. C. Gregg, R. C. Lien, and M. E. Carr, 1995: Comparison of turbulence kinetic energy dissipation rate estimates from two ocean microstructure profilers. *J. Atmos. Oceanic Technol.,* **12,** 346–365.

Mudge, T., and R. G. Lueck, 1994: Digital signal processing to enhance oceanographic observations. *J. Atmos. Oceanic Technol.,* **11,** 825–836.

Nasmyth, P., 1970: Oceanic turbulence. Ph.D. thesis, University of British Columbia, 69 pp.

Ninnis, R., 1984: The effects of spatial averaging on airfoil probe measurements of oceanic velocity microstructure. Ph.D. thesis, University of British Columbia, 109 pp.

Nortek, 1998: ADV operations manual. 1 April 1998 ed. Nortek, Oslo, Norway, 31 pp. [Available from Nortek AS, Industriveien 33, 1337 Sandvika, Norway.]

Oakey, N. S., 1982: Determination of the rate of dissipation of turbulent energy from simultaneous temperature and velocity shear microstructure measurements. *J. Phys. Oceanogr.,* **12,** 256–271.

Oppenheim, A. V., R. W. Schafer, and J. R. Buck, 1999: *Discrete-Time Signal Processing.* 2d ed. Signal Processing Series, Prentice-Hall, 858 pp.

Osborn, T. R., and W. R. Crawford, 1980: An airfoil probe for measuring turbulent velocity fluctuations in water. *Air–Sea Interaction: Instruments and Methods*, L. H. F. W. Dobson and R. Davis, Eds., Plenum, 369–386.

Panchev, S., and D. Kesich, 1969: Energy spectrum of isotropic turbulence at large wavenumbers. *C. R. Acad. Bulg. Sci.,* **22,** 627–630.

Rothchild, B. J., and T. R. Osborn, 1988: Small-scale turbulence and plankton contact rates. *J. Plankton Res.,* **10,** 465–474.

Seuront, L., F. Schmitt, Y. Lagadeuc, D. Shertzer, and S. Lovejoy, 1999: Universal multifractal analysis as a tool to characterize multiscale intermittent patterns: Example of phytoplankton distribution in turbulent coastal waters. *J. Plankton Res.,* **21,** 877–922.

Stewart, R. W., and H. L. Grant, 1999: Early measurements of turbulence in the ocean: Motives and techniques. *J. Atmos. Oceanic Technol.,* **16,** 1467–1473.

Sundby, S., 1997: Turbulence and ichtyoplankton: Influence on vertical distributions and encounter rates. *Sci. Mar.* **61,** 159–176.

Tennekes, H., and J. L. Lumley, 1972: *A First Course in Turbulence.* MIT Press, 300 pp.

Voulgaris, G., and J. H. Trowbridge, 1998: Evaluation of the acoustic Doppler velocimeter (ADV) for turbulence measurements. *J. Atmos. Oceanic Technol.,* **15,** 272–289.

Wolk, F., L. Seuront, and H. Yamazaki, 2001: Spatial resolution of a new micro-optical probe for chlorophyll and turbidity. *J. Tokyo Univ. Fish.,* **87,** 13–21. [Available from Tokyo University of Fisheries, 4-5-7 Konan, Minato-Ku, 108-8477, Tokyo, Japan.]

Yamazaki, H., 1993: Lagrangian study of planktonic organisms: Perspectives. *Bull. Mar. Sci.,* **53,** 265–278.

——, T. Osborn, and K. D. Squires, 1991: Direct numerical simulation of planktonic contact in turbulent flow. *J. Plankton Res.,* **13,** 629–643.

——, D. L. Mackas, and K. L. Denman, 2002: Coupling small-scale turbulent processes with biology. *The Sea,* A. R. Robinson, J. J. McCarthy, and B. J. Rothschild, Eds., Biological–Physical Interactions in the Ocean, Vol. 12, John Wiley and Sons, 51–112.